communications chemistry

A Nature Portfolio journal

Article

https://doi.org/10.1038/s42004-025-01533-y

Organic phosphorescence in Pt(II)-complexes linked to organic chromophores for blue-emitting organic light-emitting diodes

Seong Woon Jeong[1,5], Hyung Joo Lee[1,2,5], Bum June Park[3], Min-Jong Bong[1,2], Daehan Lee[1], Taekyung Kim[4] ✉, Chul Hoon Kim[1,2] ✉ & Ho-Jin Son[1,2] ✉

Recently, organic persistent room-temperature phosphorescence (OPRTP), entailing triplet-state emission from purely organic units instead of luminescent heavy metal complexes, has emerged as a promising alternative for the development of emitting materials in organic light-emitting diodes (OLEDs). For OPRTP-based devices to achieve acceptable performances, the low emission efficiency caused by weak spin-orbit coupling and high sensitivity to external environmental factors, such as temperature, moisture, and oxygen must be overcome. Herein, four-coordinate N-heterocyclic carbene Pt(II) complexes bearing carbazole (Cz) or naphthalene (Np) groups were assembled and found to exhibit exothermic triplet-triplet energy transfer (TTET) from the high triplet metal-to-ligand charge transfer (^{3}MLCT) state (T_1 = 2.97 eV) of the Pt core to the lower triplet states (T_1 = 2.58–2.87 eV) of the tethered organic Cz and Np moieties. The presented design strategy enables the persistent organic phosphorescence of organic molecules under ambient conditions and triplet electroluminescence of the organic group via TTET in OLED applications.

The development of organic light-emitting diode (OLED) technology has significantly transformed the display industry since Tang et al. first observed green electroluminescence in a multilayer device in 1987[1–4]. The commercialization of OLEDs, especially in displays, has benefited greatly from advancements in materials science, and in particular, with the introduction of noble metal phosphorescent emitters. These materials have substantially enhanced the electrical conversion efficiency of OLEDs, resulting in displays with a wider color gamut, richer colors, and improved image quality[4]. Notwithstanding these advancements, the ongoing development of new light-emitting materials is essential for further advances in OLED technology. A key focus area is the development of blue-light-emitting materials. Compared with their green and red counterparts, blue phosphorescent OLEDs have historically faced challenges related to their lower efficiency and shorter lifespans, which affect the overall performance and durability of OLED displays[5].

The demand for high-efficiency and long-lasting blue emitters is critical because blue light is a fundamental component of display technology. Any inefficiency in blue-light emission can negatively affect the overall energy efficiency and lifespan of the display[5–12]. Moreover, achieving blue emissions with high color purity is vital for producing accurate and vibrant colors across the spectrum. In this regard, as an alternative to the well-developed phosphorescent emitters, organic afterglow materials, including carbazole (Cz), dibenzothiophene, dibenzofuran, fluorene, and their derivatives, have been actively utilized as key units for realizing thermally activated delayed fluorescence (TADF) with the aim of maximizing exciton utilization in OLEDs[13–19]. The TADF approach focuses on minimizing the overlap between the highest occupied molecular orbital (HOMO) and the lowest unoccupied molecular orbital (LUMO) to reduce the singlet-triplet energy gap (ΔE_{ST})[18,19]. Using this approach, they achieved a remarkably low ΔE_{ST} value of 0.083 eV, while the intrinsic fluorescence efficiency exceeded 90%, and the external electroluminescence efficiency reached 19%. This innovative work paved the way for subsequent advancements in OLED technology.

On the other hand, blue phosphorescence from organic units can be efficiently achieved through intramolecular triplet-triplet energy transfer

[1]Department of Advanced Materials Chemistry, Korea University, Sejong, 30019, Republic of Korea. [2]Division of Smart Energy Convergence Engineering, Korea University, Sejong, 30019, Republic of Korea. [3]Department of Information Display, Hongik University, Seoul, 04066, Republic of Korea. [4]Department of Chemical Engineering, Kyung Hee University, Yongin, 17104, Republic of Korea. [5]These authors contributed equally: Seong Woon Jeong, Hyung Joo Lee.
✉e-mail: taekyung.kim@khu.ac.kr; chulhoon@korea.ac.kr; hjson@korea.ac.kr

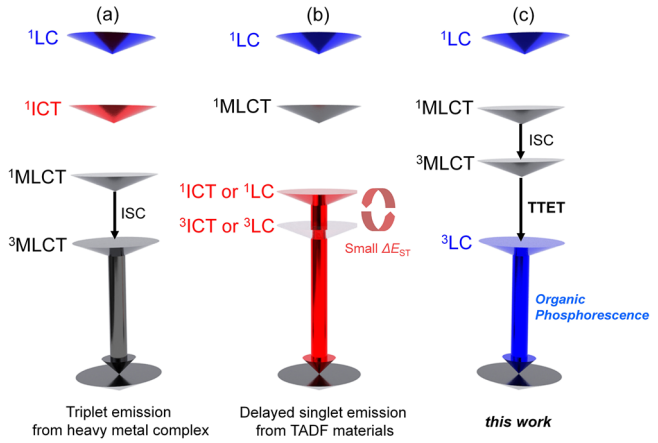

Scheme 1 | Schematic illustration of three potential arrangements of excited states. a phosphorescence from ^{3}MLCT of a heavy metal complex; **b** delayed fluorescence from TADF materials; **c** triplet ligand-centered emission (^{3}LC) via TTET. ICT and ΔE_{ST} indicate interligand charge transfer and energy gap between single and triplet ICT and LC excited states, respectively.

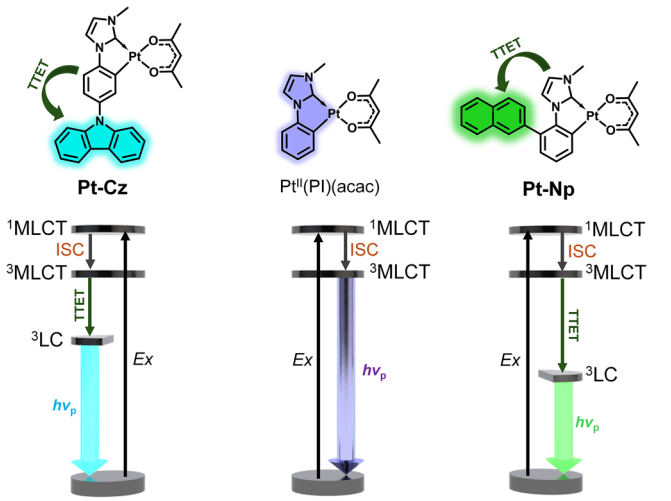

Scheme 2 | Structures and photophysical pathways of Pt(II) Complexes. Top: Chemical structures of the Pt(II) complexes—Pt^{II}(PI)(acac) (left), Pt-Cz (middle), and Pt-Np (right). Bottom: Schematic representations of the main excited-state decay pathways and the dominant emissive states for each complex.

(TTET)[20–23]. This process occurs when the triplet-excited state of a heavy-atom-containing transition metal complex transfers energy to the lower-lying triplet state of a tethered organic unit. Recent studies have demonstrated that Ir(III) complexes with two cyclometallating ligands of different energy levels (L = higher-energy ligand; L' = lower-energy ligand) can exhibit dual emissions[24–28]. These emissions arise from the higher-energy triplet metal-to-ligand charge transfer (^{3}MLCT) state and the lower-energy triplet ligand-centered (^{3}L'C) state, respectively. Notably, ^{3}L'C emission, observed as room-temperature organic phosphorescence, results from intramolecular TTET between the ^{3}MLCT and ^{3}L'C states at close proximity within the ligands bound to the Ir metal center. This TTET process is exothermic, driven by the energy difference between the high-lying ^{3}MLCT and low-lying ^{3}L'C states, leading to efficient ligand-centered triplet emission (Scheme 1). Thus, positioning an organic moiety near a high triplet energy metal-coordinated ligand facilitates efficient TTET from the donor's higher triplet state to the acceptor's lower triplet state, amplifying phosphorescence from the organic luminophore. This approach provides an effective strategy for enhancing triplet emission from various organic compounds.

Among various organic luminophores, Cz derivatives exhibit versatile utility for a range of organic electronics including OLEDs owing to their high quantum yields (Φ) and stability[13,18,29]. Notably, Cz derivatives have recently emerged as crucial building blocks in host/dopant systems and TADF materials for blue-emitting OLEDs[13,18]. However, the contribution of the phosphorescence quantum yield (Φ_P) to the overall Φ remains minimal[30]. The lowest triplet excited state of Cz derivatives, characterized by a pure $^3(\pi,\pi^*)$ configuration, has been shown to deliver persistent lifetimes[31,32]. However, because their triplet energy level is relatively high ($T_1 \approx 3.0$ eV), Cz derivatives are primarily used as host materials in the emitting layers of multi-layered OLEDs, rather than as emissive materials themselves[3,4]. Although an example of organic persistent room-temperature phosphorescence (OPRTP) using a Cz unit via intramolecular TTET has been reported, the OPRTP is only observed in the crystal or condensed phase[33]. This phase exhibits a significant redshift in the emission band to longer wavelengths ($\lambda_p \approx 500$–700 nm), contrasting with the low-temperature emission of isolated Cz units ($\lambda_{p,77\ K} \approx 480$ nm). These properties hinder processability and limit practical applications, especially as a blue-emitting material[34–37].

In this study, we designed an *N*-heterocyclic carbene (NHC)-based Pt(II) complex (Pt-Cz) by integrating an NHC-based platinum(II)-β-diketonate complex (Pt^{II}(PI)(acac), PI = phenylimidazole; acac = acetylacetone), characterized by a high triplet excited state energy[38], with an organic Cz unit with the aim of achieving persistent organic phosphorescence of Cz under ambient conditions (see Scheme 2, up). A naphthalene (Np)-substituted Pt(II) complex (Pt-Np) was also synthesized to demonstrate the broad applicability of this approach. This design strategy enabled exothermic TTET, whereby triplet excitons were transferred from the high triplet metal-to-ligand charge transfer (^{3}MLCT) state ($T_1 = 2.97$ eV) of the Pt core to the lower triplet ligand-centered (^{3}LC) states (T_1(Cz and Np) = 2.58–2.87 eV) of the appended organic Cz and Np moieties (Scheme 2). This TTET process, which differs from the typical triplet ^{3}MLCT emission of heavy metal complexes and the delayed fluorescence of TADF materials (Scheme 1), effectively enhanced the persistent ^{3}LC emission of the organic molecules (λ_p = 450–480 nm for Pt-Cz and λ_p = 480–650 nm for Pt-Np) under ambient conditions. Overall, the developed organometallic-organic hybrid system yielded efficient and long-lasting organic phosphorescence, achieving a reasonable solid-state phosphorescence quantum yields of up to 30% under ambient conditions. A multilayer OLED device doped with 5% Pt-Cz was fabricated, wherein the organic Cz tether was found to emit sky-blue phosphorescence via TTET, resulting in an external quantum efficiency (EQE) of 1.92%, current efficiency of 2.66 cd/A, and power efficiency of 1.78 lm/W. This approach provides an effective platform for the development of organic triplet emitters for OLED applications.

Results and discussion

Synthesis and characterization

Cz- or Np-substituted phenylimidazole ligands (CzPI and NpPI, respectively, where PI = phenylimidazole) were synthesized in two steps, as shown in Supplementary Scheme 1. The Cz/Np-tethered cyclometalated Pt(II) complexes (Pt(CzPI)Cl_2 and Pt(NpPI)Cl_2) were prepared via two-step metalation of the imidazolium ligand salts (CzPI$^+$ and NpPI$^+$): first, they were reacted with silver(I) oxide (Ag_2O) in 1,4-dioxane, followed by transmetalation with Pt(COD)Cl_2 in 2-ethoxyethanol. Finally, the Cz/Np-tethered Pt^{II}(PI)Cl_2 intermediates (Pt(CzPI)Cl_2 and Pt(NpPI)Cl_2) were reacted with acetylacetone (2,4-pentanedione) to yield the desired Cz/Np-tethered Pt(PI)(acac) complexes (Pt-Cz and Pt-Np) in moderate yields (19–29%) (see synthetic details in Methods). Purified Pt-Cz/Np complexes were characterized using ^{1}H/^{13}C NMR spectroscopy and high-resolution ESI-MS (Supplementary Figs. 1–8 and Supplementary Data 1–5).

The geometries of Pt-Cz and Pt-Np were determined using single-crystal X-ray crystallography; single crystals were obtained by evaporation from a DCM/*n*-hexane (v/v = 5:1) solution (Fig. 1 and Supplementary Tables 1–5). Pt-Cz and Pt-Np crystallized in a monoclinic system with space

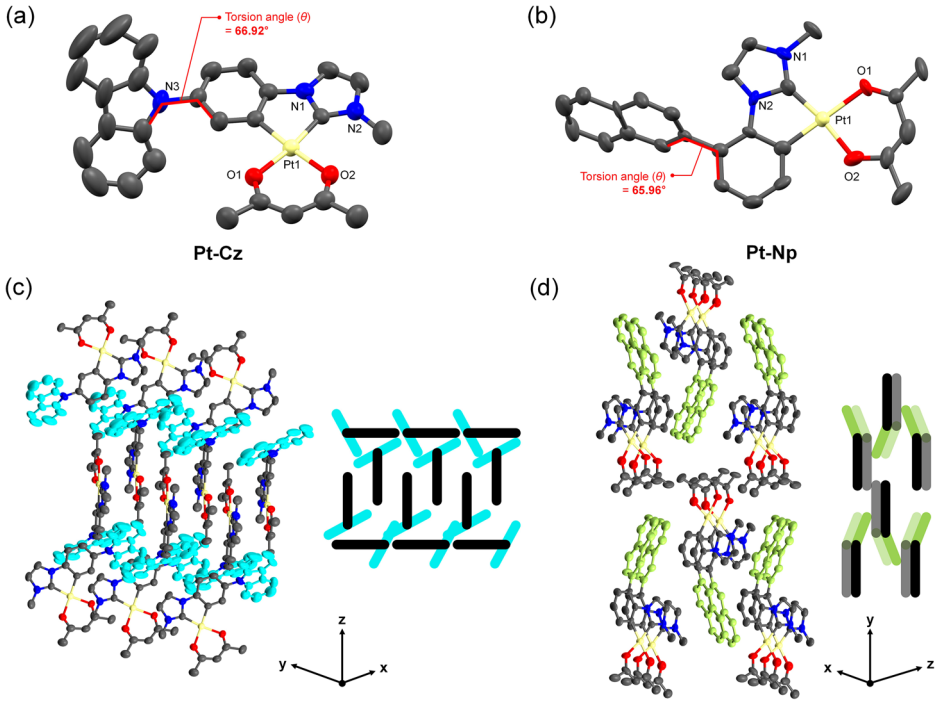

Fig. 1 | X-ray crystal structures and molecular packing of Pt(II) complexes. Top: Crystal structures of (**a**) Pt-Cz and (**b**) Pt-Np shown with thermal ellipsoids drawn at 30% probability. Bottom: Molecular packing diagrams of (**c**) Pt-Cz and (**d**) Pt-Np, illustrating key intermolecular interactions. Hydrogen atoms are omitted for clarity.

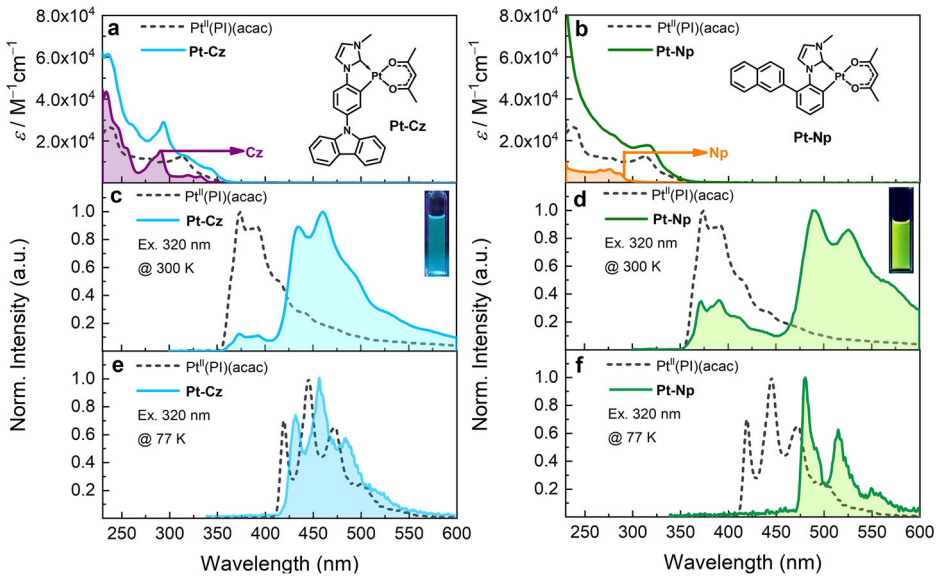

Fig. 2 | Photophysical characterization of Pt(II) complexes. Top: Steady-state UV–Vis absorption spectra (**a**, **b**) of Pt^{II}(PI)(acac), Cz, Np, Pt-Cz, and Pt-Np (10 μM in DCM). Middle: Room-temperature emission spectra (**c**, **d**) recorded in dichloromethane (DCM, 10 μM, 300 K). Bottom: Low-temperature emission spectra (**e**, **f**) measured in 2-methyltetrahydrofuran (2-MeTHF, 10 μM, 77 K).

groups $C2/c$ and $P2_1$, respectively (Supplementary Data 6 and 7). The crystallographic data for each Pt(II) complex, including the key bond distances and dihedral angles between the organic tethers (Cz and Np) and the phenyl planes of the PI ligand, are provided in Supplementary Tables 2–5. The tethered organic moieties were nearly perpendicular to the PI ligand: the dihedral angle between the plane of the substituted organic moieties (Cz or Np) and that of the Pt-coordinated PI ligand was 65–67° (Fig. 1a, b). This orthogonal geometry allows for close proximity between the Pt complex and the organic substituents, facilitating efficient triplet-triplet Dexter ET without compromising the electronic properties of the Pt complex through π-extension. It is noteworthy that, in comparison to Pt-Cz, the crystal packing geometry of Pt-Np exhibits stronger intermolecular interactions arranged in a Herringbone pattern (Fig. 1c, d). This variation significantly influences the extent of excimer formation and the structural rigidity, thereby impacting the photophysical properties of Pt(II) complexes in highly concentrated solutions and solid-state environments (*vide infra*).

Steady-state absorption and emission properties

Figure 2 shows the absorption spectra of Cz, Np, Pt^{II}(PI)(acac), and Cz/Np-substituted Pt(II) complexes Pt-Cz and Pt-Np recorded at ambient temperature (300 K) in DCM. Pristine Cz and Np displayed characteristic absorption peaks at ~290 nm ($\pi \rightarrow \pi^*$, $\varepsilon = \sim 1.5 \times 10^4\,M^{-1}\,cm^{-1}$) and 320 nm ($n \rightarrow \pi^*$, $\varepsilon = \sim 0.3 \times 10^4\,M^{-1}\,cm^{-1}$) and relatively lower absorption bands at 250–300 nm ($\pi \rightarrow \pi^*$, $\varepsilon = \sim 0.8 \times 10^4\,M^{-1}cm^{-1}$), respectively. For Pt^{II}(PI)(acac), the intense band near 312 nm and the weaker absorption in the 315–350 nm range were attributed to the ligand-centered (^{1}LC, $\pi \rightarrow \pi^*$) transition of the PI ligand and the mixed singlet MLCT (^{1}MLCT) transition, respectively[38]. The absorption spectra of the Pt-Cz and Pt-Np compounds

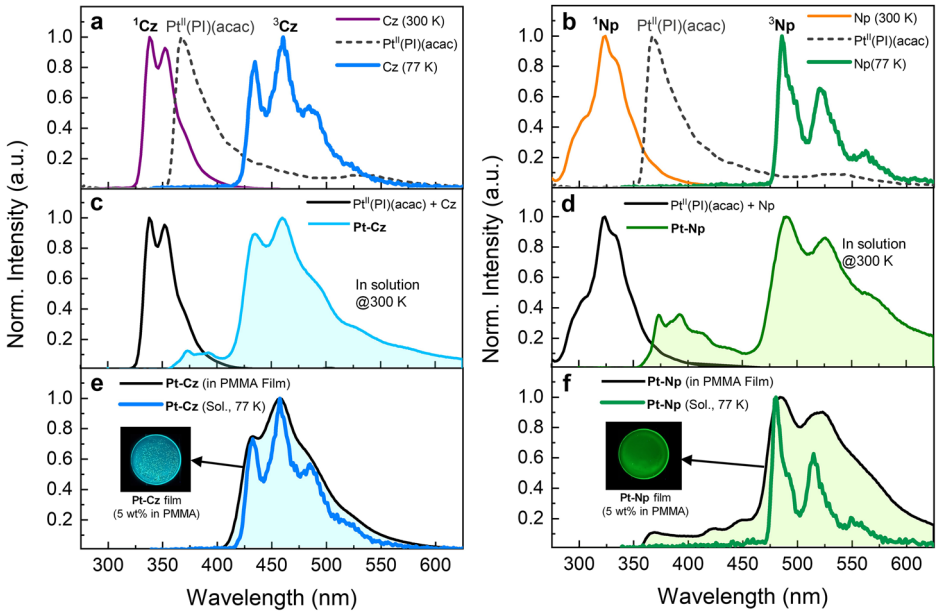

Fig. 3 | Steady-state emission spectra of Pt(II) complexes under various conditions. Top: Emission spectra of Pt^{II}(PI)(acac), Cz, and Np (10 μM) recorded (**a**) in dichloromethane (DCM) at 300 K and (**b**) in 2-methyltetrahydrofuran (2-MeTHF) at 77 K. Middle: Comparative emission spectra of Pt-Cz and Pt-Np along with reference compounds (Pt^{II}(PI)(acac), Cz, and Np), measured in DCM at 300 K (**c**, **d**). Bottom: Emission spectra of Pt-Cz and Pt-Np embedded in PMMA films (5 wt% Pt(II) complex) at 300 K (**e**), and in 2-MeTHF at 77 K (**f**).

Table 1 | Photophysical data of Pt(II) complexes

Complex	At 300 K[a]			In film[c]		At 77 K[d]
	Abs (λ_{abs}/nm)	Em (λ_{em}/nm)	Φ_{em}[b] (%)	Em (λ_{em}/nm)	Φ_{em}[b] (%)	Em (λ_{em}/nm)
Pt^{II}(PI)(acac)	239, 277, 312, 337	374, 392	2.7	420, 442, 467	20.5	418, 445, 471
Pt-Cz	236, 260, 293, 318, 343	374, 392, 434, 460	1.4	431, 458	30.0	432, 457, 484
Pt-Np	281, 317, 339	374, 392, 492, 526	1.0	522	3.7	479, 514

[a]Values were obtained in Ar-saturated dichloromethane (10 μM) at 300 K. [b]Quantum yields were measured using a Quantaurus-QY system (λ_{ex} = 320 nm). [c]Films were fabricated on fused silica glass substrates (5 wt% Pt(II) complex) using poly(methyl methacrylate) (PMMA) dissolved in toluene. [d]Values obtained in 2-methyltetrahydrofuran (2-MeTHF) glassy matrix at 77 K.

contained the absorption features of both the Pt core and the organic tethers (Cz and Np). The distinct absorption bands observed at ~280 nm and in the 315–350 nm range can be attributed to spin-allowed singlet π–π^* transitions and ^{1}MLCT transitions, respectively. The red shift in the ^{1}MLCT band of the Cz- and Np-tethered Pt(II) complexes compared to that of the pristine Pt^{II}(PI)(acac) complex likely originated from the π-extension of the PI ligand caused by the attachment of these organic moieties. Pt-Cz exhibited a slightly red-shifted ^{1}MLCT absorption band (~340 nm) compared to that of Pt-Np (~322 nm). This shift suggests that the extent of π-extension is influenced by both the dihedral angle between the Cz/Np ring and the phenyl plane in the PI ligand (60–67° for Pt-Cz and 65–67° for Pt-Np), as well as the electronic structure of the substituted organic groups.

Figure 3 shows the photoluminescence (PL) spectra of Pt-Cz and Pt-Np obtained in DCM at 300 K and in 2-MeTHF at 77 K, along with the fluorescence emission spectra of the reference compounds (pure Np/Cz and pristine Pt^{II}(PI)(acac)). At 300 K, Cz and Np exhibited characteristic fluorescence emissions at ~360 nm and ~350 nm, respectively, while the deep blue phosphorescence emission of Pt^{II}(PI)(acac) was observed in the range of 360–430 nm. As shown in Fig. 3c, Pt-Cz exhibited two distinct emission bands at ~370 and 470 nm (extending to 600 nm). These bands correspond to the phosphorescent emission of the core Pt(II) complex and the triplet ligand-centered (^{3}LC) emission of the Cz moiety, respectively, based on their correlation with the 77 K emissions of Pt^{II}(PI)(acac) and the pure Cz moiety. In this study, to prevent co-excitation of the Cz unit, an excitation wavelength of 350 nm was used as it does not overlap with the absorbance of Cz. Therefore, the observation of ^{3}LC emission from the Cz unit without direct excitation can be explained by TTET from the ^{3}MLCT of the core Pt(II) complex to the ^{3}LC of the tethered Cz. The results show that the intramolecular TTET process (Pt(II) core → Cz or Np) is dominant in Pt-Cz and Pt-Np.

The TTET emission mechanism was further supported by the results of comparative PL experiments using Pt-Cz and a mixed sample (Pt^{II}(PI)(acac) + Cz) (Fig. 3c). Under excitation at 350 and 250 nm, the mixed sample exhibited only the Pt(II) complex phosphorescence and the local fluorescence of the Cz unit (λ_f = ~350 nm), respectively, indicating that energy transfer did not occur between the components. In contrast, the combined Pt-Cz complex consistently showed dual phosphorescent emissions originating from the ^{3}MLCT of the core Pt(II) complex and the ^{3}LC of the appended Cz unit. This phenomenon clearly indicates that a direct connection between the Pt(II) complex and Cz unit is essential for efficient TTET from the former to the latter. Pt-Np exhibited similar behavior in analogous experiments, displaying distinct green photoluminescence originating from the ^{3}LC of the Np substituent, whereas the mixed sample (Pt^{II}(PI)(acac) + Np) showed only Np fluorescence at an excitation wavelength of 250 nm and only blue phosphorescence of the Pt(II) complex at an excitation wavelength of 350 nm (Fig. 3d). These results indicate that the TTET from the Pt core to the organic tethers (Cz or Np) occurred only in Pt-Cz and Pt-Np where the Pt(II) core is directly connected to the organic units.

At 77 K, Pt-Cz and Pt-Np exhibited structured emissions (Fig. 3e, f). Unlike the phosphorescence of Pt^{II}(PI)(acac) at 77 K (λ_p = 385 nm), Pt-Cz and Pt-Np displayed more red-shifted emissions that closely matched the phosphorescence spectra of the Np and Cz units at 77 K. These results suggest that the ^{3}MLCT state electrons of the Pt-Cz and Pt-Np complexes were quenched toward the ^{3}LC state of the adjacent organic tethers (Cz and Np). This hypothesis was further corroborated by the time-resolved optical spectroscopy results (see below).

Interestingly, as shown in Table 1, the solidified Pt(II) complexes (5 wt% in poly(methyl methacrylate) (PMMA) polymer films) exhibited significantly improved emission efficiencies (Φ_{em}) compared to those obtained in solution at 300 K. Additionally, unlike the dual emission (^{3}MLCT and ^{3}LC) observed

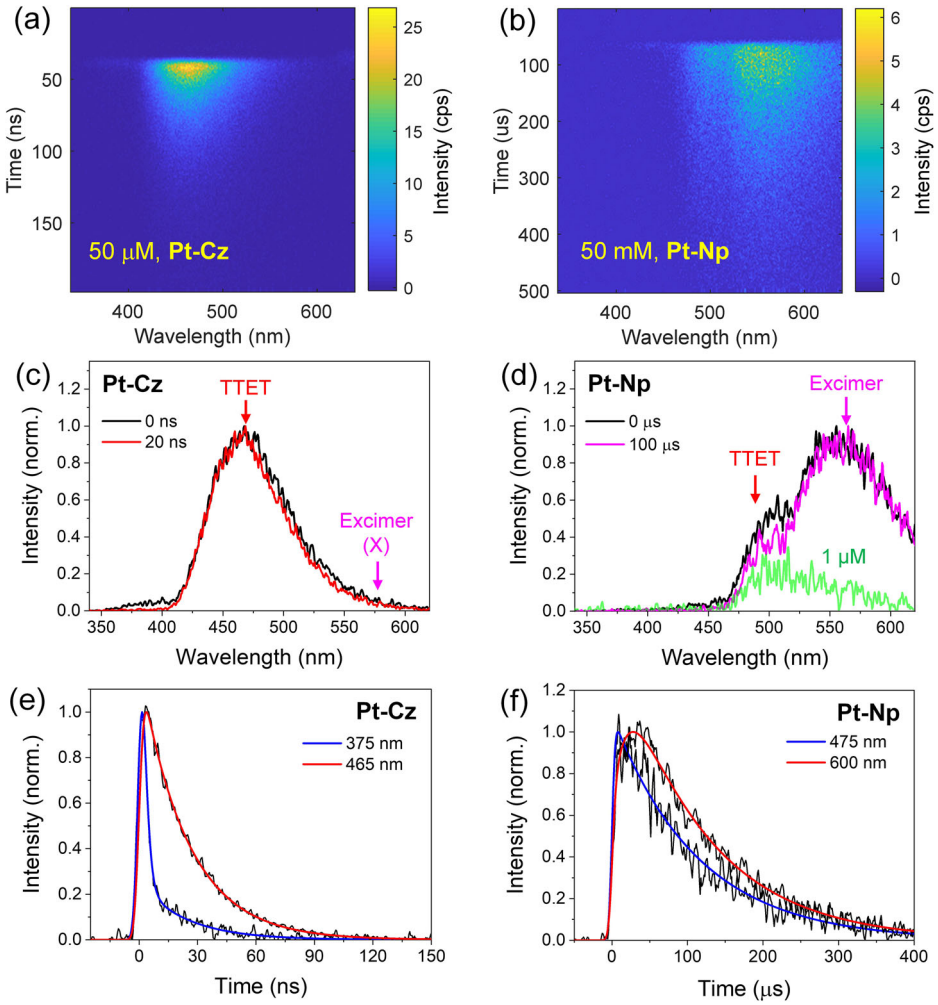

Fig. 4 | Time-resolved photoluminescence (TRPL) analysis of Pt-Cz and Pt-Np in solution. Top: Raw TRPL contour images of (**a**) Pt-Cz and (**b**) Pt-Np (50 μM in DCM), where the vertical color bar indicates the PL intensity in counts per second (cps). Middle: TRPL spectra at two representative time-delays (**c**, **d**) compared with the PL spectrm of highly diluted Pt-Np solution (1 μM; green curve). Bottom: TRPL decay profiles at selected blue and red spectral regions (**e**, **f**); their multi-exponential fitting results are listed in Supplementary Table 6.

in the solution phase, which indicates partial TTET (Pt(II) → Cz or Np), the rigidified Pt(II) complexes in the PMMA film predominantly exhibited ^{3}LC emissions from the Cz or Np moiety with minimal ^{3}MLCT emission from the core Pt^{II}(PI)(acac) complex (Fig. 3e, f). This may indicate a substantial improvement in the TTET efficiency from the ^{3}MLCT state of the core Pt(II) site to the ^{3}LC state of the organic peripheral groups and/or the activation of the ultrafast TTET process followed by prolonged population relaxations of the product ^{3}LC state in the glassy polymer film[39]. This hypothesis was further verified with the time-resolved optical spectroscopy results (*vide infra*).

The substantial decrease in the emission intensities of Pt-Cz and Pt-Np at 430–460 nm and 480–600 nm, respectively, in the presence of oxygen gas (Supplementary Fig. 9) indicated that the emissions originated from the relatively low triplet excited state (^{3}[Cz]* or ^{3}[Np]*) of the respective organic tether. The origin of the red-shifted emission of the Cz/Np-tethered Pt(II) complexes was further investigated by obtaining their PL excitation spectra at their respective emission wavelength (λ_{em} = 450 nm for ^{3}[Cz]* and 530 nm for ^{3}[Np]*). As shown in Supplementary Fig. 10, the PL excitation spectra of both Pt-Cz and Pt-Np show distinct bands in the 280–350 nm range, corresponding to the ^{3}MLCT absorption of the core Pt^{II}(PI)(acac) unit (see inset of Supplementary Fig. 10 and the absorption spectra in Fig. 2). This further confirmed that the organic phosphorescence emissions of Pt-Cz and Pt-Np occurred through TTET from the high-lying triplet excited state of the Pt(II) core to the low-lying ^{3}[Cz]* or ^{3}[Np]* states.

TTET dynamics probed by time-resolved optical spectroscopy

The TTET process between the core Pt(II) complex and organic tethers (Cz and Np) was investigated using time-resolved photoluminescence (TRPL) spectroscopy. Figure 4 shows the TRPL spectral images of the two samples in solution (50 μM). For both samples, the PL band of the Pt(II) core around 400 nm was quenched instantaneously, followed by the appearance of an amplified red-shifted PL band at wavelengths >420 nm from the peripheral organic group. Interestingly, Pt-Cz shows a single TTET-induced PL band at ~465 nm, whereas Pt-Np contains two PL bands at 500 and 570 nm. It should be noted that the planar structure of Pt^{II}(PI)(acac) facilitates excimer formations in concentrated solutions, which competes with intramolecular population transfer processes such as TTET. Therefore, the two convoluted PL bands of Pt-Np could be attributed to these competing processes. To explore this further, we examined the intrinsic photophysical properties of pristine Pt^{II}(PI)(acac) by obtaining its PL spectra varying concentrations. As shown in Supplementary Fig. 1a, b, the red-shifted PL band at 570 nm was strongly dependent on the concentration of the Pt^{II}(PI)(acac) solution, whereby no excimer emission was noted for the highly diluted Pt^{II}(PI)(acac) solution (1 μM). Considering this, the red-shifted PL band around 460–510 nm in the dilute Pt-Cz and Pt-Np solutions (1 μM) can be attributed to the TTET-induced emission of the corresponding organic tether group (Supplementary Fig. 1c, d). This confirms that the TTET process in Pt-Np is indeed feasible. However, its ultrafast time-scale, observed in the region of the ^{3}MLCT emission (λ_{em} = 375–435 nm in Supplementary Table 6), is limited by the instrument response function (IRF) of the streak-scope setup. Accurate determination of this process requires femtosecond transient absorption spectroscopy (*vide infra*).

To systematically investigate the excimer formations of Pt-Cz and Pt-Np in solution, the steady-state PL spectra of the two samples were recorded with varying concentrations (1 μM ~ 1 mM) (Supplementary Fig. 12). For

comparison, steady-state PL spectra of their crystalline forms were also recorded to get insights into excimer formation in extended oligomeric aggregates. Pt-Cz solutions displayed nearly identical emission features around 465 nm (^{3}LC) with negligible excimer band at 570 nm across a wide concentration range (1 μM to 1 mM). The fully red-shifted excimer band was observed only in its crystalline state. The predominant generation of the ^{3}[Cz]* state in solution indicates that the perpendicular geometry of the appended Cz moiety effectively prevents intermolecular stacking interactions even in the highly concentrated solution (>50 μM). Consequently, the apparent red-shifted PL band by the ultrafast TTET process can be exclusively observed in Pt-Cz, as shown in Fig. 4c. On the other hand, the short PL lifetime of ~24 ns at 465 nm (see Supplementary Table 6) indicates that flexible skeletal motions of Pt-Cz in the excited state cause rapid non-radiative relaxations of the ^{3}[Cz]* state[39]. This is further supported by the prolonged PL lifetime of the ^{3}LC state in a glassy polymer matrix (*vide infra*). The strong intermolecular interactions in Pt-Np are further corroborated by the pronounced change in the excimer band with increasing concentration and its resemblance to the single PL band at 570 nm observed in the crystalline state. That is, the Np group plays a key role in inducing more rigid and extended H-type molecular aggregates in solution. In this context, the formation of the well-stacked aggregates should be responsible for the prolonged PL lifetimes (>100 μs) of both ^{3}LC and excimer states in the concentrated solution (50 μM) (Fig. 4f).

The photophysical properties of the Pt core, Pt^{II}(PI)(acac), were further examined in PMMA thin film and crystalline form using TRPL spectra measurements (Supplementary Figs. 13–14 and Table 7). In the PMMA film (5 wt%), the excimer emission at 550 nm was not discernible even in the time-domain measurement, which is consistent with the steady-state spectrum shown in Fig. 3e. The TRPL profile of the thin film at 450 nm revealed diverse population relaxations, including an additional slow decay component of 3.41 μs, whereas the diluted solution (1 μM) showed a monotonic PL decay (1.1 μs) with negligible spectral change (Supplementary Tables 6–7). This suggests that Pt^{II}(PI)(acac) monomers are more likely to be isolated within the PMMA matrix, and some conformers become further rigidized to give the longer PL lifetime. In the crystalline phase, the sample exhibits the apparent excimer band at 550 nm with diverse population decays exceeding 25 μs, similar to the observations in the concentrated solution (50 μM, see Supplementary Fig. 11b). Thus, we conclude that the low dopant concentration of 5 wt% in the PMMA matrix is insufficient to facilitate the formation of Pt^{II}(PI)(acac) excimers. Instead, well-stacked oligomeric aggregates are more favorable in the concentrated solution (50 μM) and crystalline form.

The PL intensity ratio between the ^{3}MLCT (~375 nm) and ^{3}LC (465 nm) states for Pt-Cz in solution was also sensitive to its concentration (Supplementary Fig. 12a). The PL intensity of the Pt core (^{3}MLCT) was moderate in the diluted solution (1 μM), but highly diminished in concentrated solutions above 50 μM, resulting in the relatively strong PL spectrum of the TTET-induced ^{3}[Cz]*. Similarly, the PMMA film (5 wt%) also exhibited strong ^{3}LC emission with negligible ^{3}MLCT one (Fig. 3e). Note that the PL lifetime of the ^{3}LC state at 450 nm was 4.7 ns (~80% in amplitude), 24.2 ns for the dilute (1 μM) and concentrated (50 μM) solutions, respectively, and increased significantly (>850 ns) in the polymer matrix (Supplementary Figs. 13–14 and Tables 6-7). These experimental results suggest that the enhanced PL intensity of the ^{3}LC state in the thin film, along with negligible ^{3}MLCT emission, primarily arises from the prolonged lifetimes of the ^{3}LC state (additionally, the TTET process may be partially affected by the structural confinement in the polymer matrix). That is, flexible skeletal motions of Pt-Cz in the excited state, which lead to rapid deactivation of the ^{3}LC state, are responsible for the short lifetime observed in the diluted solution. These fast non-radiative pathways can be effectively suppressed in the glassy polymer matrix. Accordingly, in the concentrated solution (50 μM), the solvated Pt-Cz may experience weak conformational confinements from long-range intermolecular interactions, leading to the disappearance of the fast decay component (~4.7 ns).

The excited state dynamics of Pt-Np in condensed phase was highly complicated by the formation of molecular aggregates facilitated by the organic tether moieties (Supplementary Figs. 13–14 and Tables 6-7). As shown in Fig. 4d, the Pt-Np solution revealed the strong ^{3}LC and excimer emissions due to effective stacking interactions in the aggregates. Notably, the PL lifetimes of both ^{3}LC and excimer states were rather longest (>100 μs) in the concentrated solution (50 μM) than in the crystalline form. In the crystal, the PL lifetime of the ^{3}LC state at 475 nm was ~250 ns, while the 2nd and 3rd time constants (~10–16 μs) were attributed to spectral overlap of the strong excimer emission at 600 nm. This is in sharp contrast to Pt-Cz, where the ^{3}[Cz]* product in solution undergoes the relatively fast deactivation (~24 ns) compared to that in the solid-state samples. According to the packing structure of Pt-Np crystal in Fig. 1d, the herringbone arrangements of fully-stacked Pt-Np dimeric units in the crystal may impede strong excitonic interactions across the extended spatial domain. In this context, we argue that extended H-type molecular aggregates with a long coherence length are favorable in solution, thereby reducing oscillator strengths of the optical transitions and suppressing structural distortions. It is noteworthy that the spectral width of the excimer PL band at 570 nm gradually decreased with increasing concentration (Supplementary Figs. 12b), implying that effective and extended stacking interactions in solution promote the formation of a well-ordered aggregate with reduced conformational disorder. On the other hand, in the PMMA film (5 wt%), the PL lifetime at 475 nm was similar to that at 600 nm, and only an extremely weak PL with a time-constant of 230 μs was detected at 600 nm (Supplementary Table 7), indicating negligible excimer emission. Again, this confirms that the dopant concentration of 5 wt% is sufficiently low to minimize excimer formation in the thin film.

The excimer formation kinetics of Pt-Np in the concentrated solution (50 μM) and crystalline form can be exclusively resolved at the red-side of the PL band (λ_{em} = 600 nm) (Fig. 4f and Supplementary Fig. 14). In solution, the TTET process occurs instantaneously (limited by the IRF), but the excimer formation appears to be a delayed dynamic process of molecular excitons, as evidenced by the slow rise component of 17.9 μs at 600 nm (Supplementary Table 7). The origin of the slow-rise is unclear but may be associated to the excitonic dynamics occurring in the highly extended oligometric aggregates with conformational heterogeneities because the crystalline form rather showed a relatively fast rise of 1.82 μs. Further experiments are currently underway to elucidate the slow excitonic dynamics of Pt-Np in these extended systems.

Next, the TTET processes of the Pt(II) complexes were investigated using femtosecond transient absorption (TA) spectroscopy. Figure 5 shows the TA spectra of Pt-Cz and Pt-Np in solution (50 μM) and the corresponding evolution-associated spectra (EAS). As the time delay increased, the absorption bands at 700 and 430 nm gradually increased for Pt-Cz and Pt-Np, respectively. As shown in Supplementary Figs. 15, the Pt(II) core (Pt^{II}(PI)(acac)) alone did not undergo any significant spectral changes, however, the two hybrid samples exhibited characteristic spectral evolutions with a slow rise component of 10 ~ 16 ps. To quantitatively determine the TTET kinetics, the TA spectra were spectrally deconvoluted using the EAS analysis as described elsewhere[40]. Here, we assumed that the TTET reaction follows first-order serial kinetics, as shown below.

$$S_1 \xrightarrow{\tau_{ISC}} S_2 \xrightarrow{\tau_{TTET}} S_3 \xrightarrow{\tau_D} GS \quad (1)$$

where S_1, S_2, and S_3 correspond to the ^{1}MLCT of Pt^{II}(PI)(acac), ^{3}MLCT of Pt^{II}(PI)(acac), and ^{3}[Np or Cz]* states, respectively. GS denotes the ground state. The ultrafast intersystem crossing (ISC) process was included in the kinetic model for Pt-Np, but omitted for Pt-Cz because of the negligible population changes near time-zero, caused by the strong spectral overlap between the reactant and product states (see Supplementary Figs. 15b). Moreover, the excimer formation pathway of Pt-Np was not considered because its timescale (17.8 μs) extends far beyond the experimental time window (3 ns) of the TA setup. As shown in Fig. 5, the TTET processes depicted in the TA spectra were quantitatively resolved via global EAS

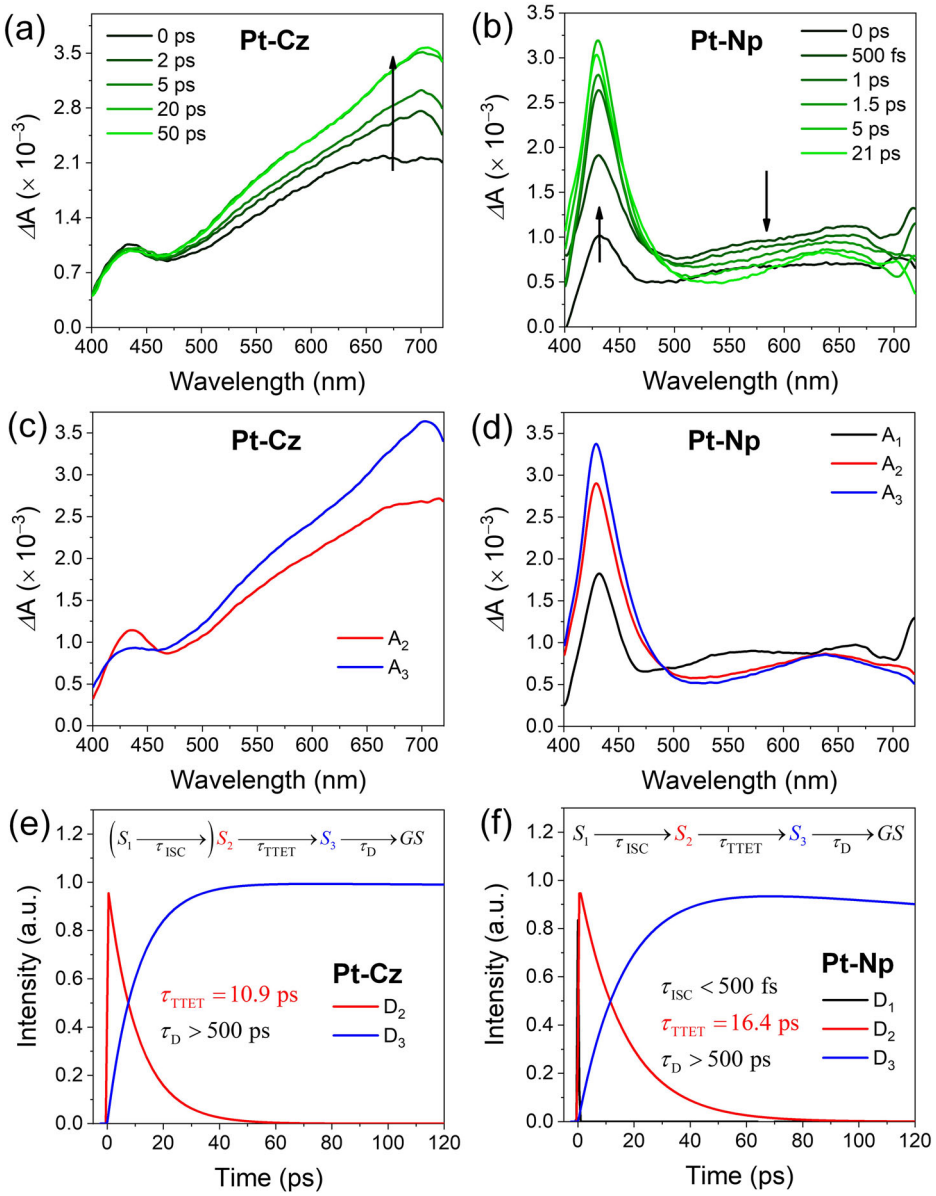

Fig. 5 | Femtosecond transient absorption (TA) spectroscopy and kinetics of Pt-Cz and Pt-Np. Top: TA spectra of (**a**) Pt-Cz and (**b**) Pt-Np (50 μM in DCM) with corresponding evolution-associated spectra (EAS). Bottom: Principal spectral components (*A* terms) (**c**) Pt-Cz and (**d**) Pt-Np derived from a sequential kinetic model and their associated population kinetics (*D* terms) (**e**) Pt-Cz and (**f**) Pt-Np representing transient species (S_1, S_2, S_3).

analysis with the evolution-associated *A* (spectra) and *D* (population kinetics) terms. Here, the excited state population transfer of the ^{3}MLCT of Pt^{II}(PI)(acac) can be monitored by observing the decay of the S_2 state (D_2 term) and the corresponding rise of the S_3 state (D_3 term). The fast TTET processes, with the time-constants of ~10–16 ps (τ_{TTET}), were consistent with the TRPL results, where the PL band for the S_2 state at 400 nm was quenched instantaneously (see Fig. 4 and Supplementary Table 6).

Electrochemical properties

The electrochemical properties of all the Pt(II) complexes, including the pristine Pt^{II}(PI)(acac) complex, were studied using cyclic voltammetry (CV) in anhydrous DCM saturated with argon. Measurements were conducted relative to an internal ferrocenium/ferrocene (Fc^+/Fc) reference. At a scan rate of 100 mV s^{-1}, quasi-reversible oxidation peaks were observed in the 0.03–1.0 V range (see Table 2 and Supplementary Fig. 16). No reduction peaks were detected for any of the Pt(II) complexes, likely because of the limited working potential window in DCM. The HOMO and LUMO energy levels were calculated using E_{HOMO} (eV) = –e(E_{ox} + 4.8) and $E_{LUMO} = E_{HOMO} + E_g$, where the optical band gap (E_g) was derived from the energy at the absorption band edge. Overall, compared to the reference Pt^{II}(PI)(acac) complex, the Cz/Np-tethered Pt(II) complexes exhibited relatively lower HOMO and LUMO energy levels, indicating that the substituted organic moieties influenced the electronic structure of the Pt(II) complexes (Fig. 6).

Table 2 | Electrochemical properties of Pt(II) complexes

	E^{ox}_{onset} (V)[a]	E_g (eV)[b]	E_{HOMO} (eV)[c]	E_{LUMO} (eV)[c]
Pt^{II}(PI)(acac)	0.15	3.42	–4.95	–1.53
Pt-Cz	0.41	3.36	–5.21	–1.85
Pt-Np	0.16	3.34	–4.96	–1.62

[a]The three Pt(II) complexes exhibited irreversible or quasi-reversible oxidation peaks. For comparison, the HOMO energy levels were determined from the first-onset oxidation potentials (E^{ox}_{onset} V vs. Fc/Fc^+). [b]E_g values were calculated using the wavelength at which the absorption band starts (E_g = 1240/λ (in nm)). [c]HOMO and LUMO energies were determined using the following equations: E_{HOMO} (eV) = $-e(E^{ox}_{onset} + 4.8)$ and $E_{LUMO} = E_{HOMO} + E_g$.

Density Functional Theory (DFT) calculations

DFT and time-dependent DFT (TD-DFT) calculations were performed to further explore the relationship between the photophysical properties

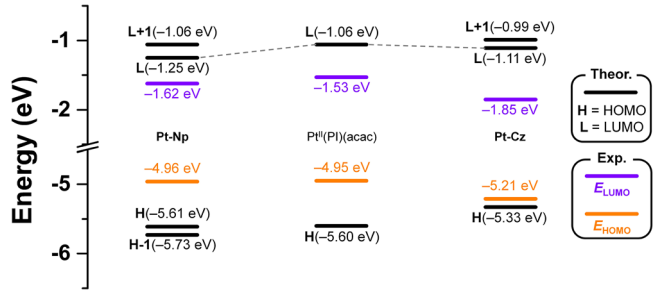

Fig. 6 | Energy level diagrams of Pt(II) complexes. Calculated molecular orbital energy levels obtained from density functional theory (DFT, black solid lines) and experimentally determined HOMO (orange solid line) and LUMO (purple solid line) levels of the three Pt(II) complexes.

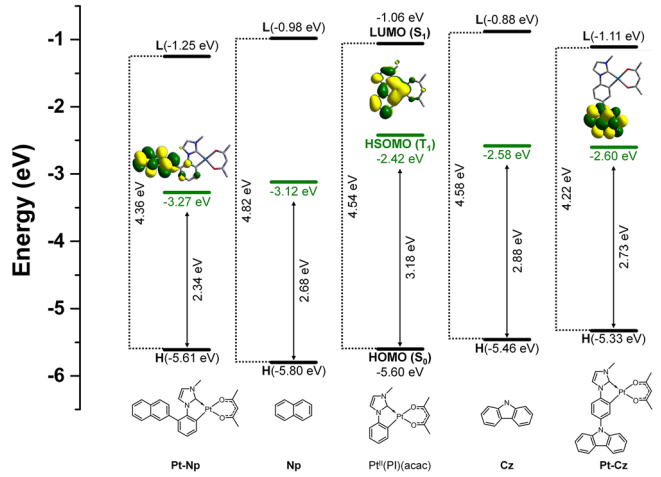

Fig. 7 | Molecular orbital energy levels of Pt(II) complexes and organic fragments. Calculated frontier molecular orbital energies of Pt(II) complexes (Pt^{II}(PI)(acac), Pt-Cz, and Pt-Np) and individual organic fragments (Np and Cz): LUMO (L, black solid line), HSOMO (green solid line), and HOMO (H, black solid line).

and electronic structures of Pt(II) complexes (Supplementary Data 8-12). Figure 7 shows the calculated and spectroscopic energies (S_0, S_1, and T_1 states) of the individual fragments (Pt(II) core, Np, and Cz) and the Cz/Np-tethered Pt(II) complexes. The results indicate that the energy levels of the organic tethers (Np and Cz) are lower than that of the Pt^{II}(PI)(acac) core, which is consistent with the experimentally observed trend in the low-temperature phosphorescence spectra (T_1 = 2.97 eV for Pt^{II}(PI)(acac) > 2.95 eV for Cz > 2.61 eV for Np). This trend aligns well with the calculated energies for the Cz/Np-substituted Pt(II) complexes and the pristine Pt^{II}(PI)(acac) complex ($\Delta E(S_0–T_1)$ = 3.18 eV for Pt^{II}(PI)(acac) > 2.73 eV for Pt-Cz > 2.34 eV for Pt-Np). Thus, Dexter-type energy transfer from the Pt(II) core to the organic tethers (Cz or Np) is energetically feasible. To gain a deeper understanding of the lowest excited-state configuration, we calculated the highest singly occupied molecular orbitals (HSOMOs), lowest singly occupied molecular orbitals (LSOMOs), and spin densities using the unrestricted hybrid functional UB3LYP method. In the Cz/Np-tethered Pt(II) complexes, the calculated HSOMOs are mainly localized on the organic tethers (Cz and Np), whereas the LSOMOs are associated with the Pt(II) metal and PI ligand. The HSOMOs are at lower energy levels compared to those of the pristine Pt^{II}(PI)(acac) complex, likely due to slight π-extension between the organic tethers and the PI ligand, which is in agreement with the electrochemical results (Table 2). Furthermore, for both Pt-Cz and Pt-Np, the triplet spin density is concentrated on the organic substituents, while the electron density remains centered on the Pt(II) core (Supplementary Fig. 17). This distribution indicates that energy transfer from the Pt(II) core to the organic tethers is achievable in the excited triplet state.

Energy transfer mechanisms

Figure 8 illustrates the relative energy levels of the excited states of all the Pt(II) complexes, including the singlet and triplet MLCT states (Pt-Cz/Np and Pt^{II}(PI)(acac)), ligand-centered (LC) states (Cz and Np), and the ET pathways for ISC and TTET within these states. In the singlet states, the energy levels of the excited singlet states of the organic tethers (^{1}[Cz]* and ^{1}[Np]*) are higher than those of the ^{1}MLCT state of the core Pt(II) complex, as indicated by the shorter wavelengths of the π–π* absorption bands of Cz and Np compared to the ^{1}MLCT absorption bands of Pt^{II}(PI)(acac). The ^{1}LC states are also located at higher energy levels than the ^{3}MLCT states, as evidenced by the shorter wavelengths of the fluorescence emissions of the organic tethers (λ_f = 356 nm for Cz and 340 nm for Np) compared to the phosphorescence emission of Pt^{II}(PI)(acac) (λ_p = 370 nm). In terms of the comparison between ^{3}LC and ^{3}MLCT, the longer wavelength phosphorescence emission of the Cz and Np units (λ_p = 406 nm for Cz and 469 nm for Np) suggests that the excited triplet states of the organic substituents are at lower energy levels than the ^{3}MLCT state. Based on these findings, the energy levels are arranged in the following order: ^{1}LC > ^{1}MLCT > ^{3}MLCT > ^{3}LC (see Fig. 8).

Upon photo-excitation of the pristine Pt^{II}(PI)(acac) complex (Fig. 8), the ^{1}MLCT state is initially populated, followed by rapid ISC induced by the strong spin-orbit coupling of the heavy Pt atom. This process results in the formation of the ^{3}MLCT state within 500 fs. At 300 K, Pt^{II}(PI)(acac) in diluted solution (1 μM) exhibits phosphorescence from the ^{3}MLCT state, with the PL lifetime of 1.1 μs, as determined from the TRPL experiments (Supplementary Table 6). In the Cz/Np-tethered Pt-Cz and Pt-Np complexes, photoirradiation generates singlet excited states (^{1}MLCT) within the Pt(II) core complex. These ^{1}MLCT states undergo ISC in both Pt-Cz and Pt-Np to form the ^{3}MLCT state within <500 fs for both Pt-Cz and Pt-Np solutions. Subsequent triplet–triplet Dexter energy transfer occurs from the ^{3}MLCT state of the Pt^{II}(PI)(acac) core to the ^{3}LC (^{3}[Cz]* or ^{3}[Np]*) of the neighboring organic tethers. Based on femtosecond TA measurements, the Dexter energy transfer rates for Pt-Cz and Pt-Np were determined to be 10.9 and 16.4 ps, respectively. The phosphorescence lifetimes (τ_{em}) in the final ^{3}LC states were measured as 24.2 ns for Pt-Cz and >100 μs for Pt-Np (50 μM).

Device performance

To evaluate the possibility of using an organic triplet emitter as a phosphorescent dopant in an actual OLED device, Pt-Cz-doped OLED devices were assembled with the following device specifications: ITO (150 nm)/BCFN:NDP-9 (10 nm, 3 wt%)/BCFN (60 nm)/SiCzCz (5 nm)/TSPO1:Pt-Cz (30 nm, 5%)/TSPO1 (5 nm)/TPBi (30 nm)/Liq (1.5 nm)/Al (100 nm), where BCFN is *N*-([1,1′-biphenyl]-4-yl)-9,9-dimethyl-*N*-(4-(9-phenyl-9H-carbazol-3-yl)phenyl)-9H-fluoren-2-amine, SiCzCz is 9-(3-(triphenylsilyl)phenyl)-9H-3,9′-bicarbazole, TSPO1 is diphenyl[4-(triphenylsilyl)phenyl] phosphine oxide, TPBi is 2,2',2"-(1,3,5-Benzinetriyl)-tris(1-phenyl-1-H-benzimidazole) and Liq is 8-quinolinolato lithium.

Figure 9 shows the chemical structures and energy levels of the OLED device components. First, a 10 nm layer containing 3% NDP-9 mixed with BCFN was assembled. This lowers the driving voltage of the device by facilitating hole movement into the hole-transporting layer (BCFN). TSPO1, which has a high energy level (T_1 = 3.36 eV), was used in the light-emitting layer to facilitate efficient energy transfer to the Pt-Cz dopant[41]. Additionally, SiCzCz and TSPO1 were placed on either side of the light-emitting layer (TSPO1) to prevent exciton formation at the BCFN/EML and EML/TPBi interfaces, which ensures that the carriers remain inside the Pt-Cz-doped layer. TPBi and Liq were used for transporting and injecting electrons into the device, respectively. The device performance parameters are provided in Supplementary Table 8.

Figure 10 shows the current density (*J*)-voltage (*V*)-luminance (*L*), current efficiency (CE)-current density (*J*), power efficiency (PE)-current density (*J*), and external quantum efficiency (EQE)-current density (*J*) curves for the device. The Pt-Cz-doped device (5%) displayed sky-blue to

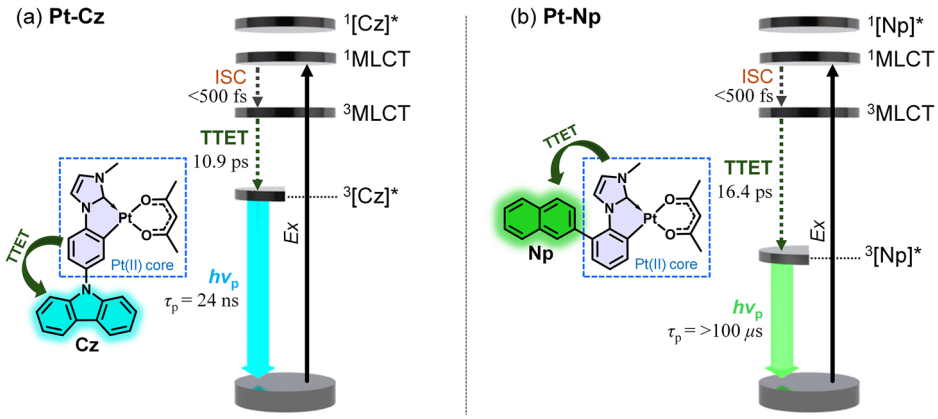

Fig. 8 | Triplet excited-state dynamics and energetics of Pt-Cz and Pt-Np. Schematic representation of the energetics and excited-state dynamics occurring in (**a**) Pt-Cz and (**b**) Pt-Np complexes in solution (50 μM), highlighting key photophysical processes.

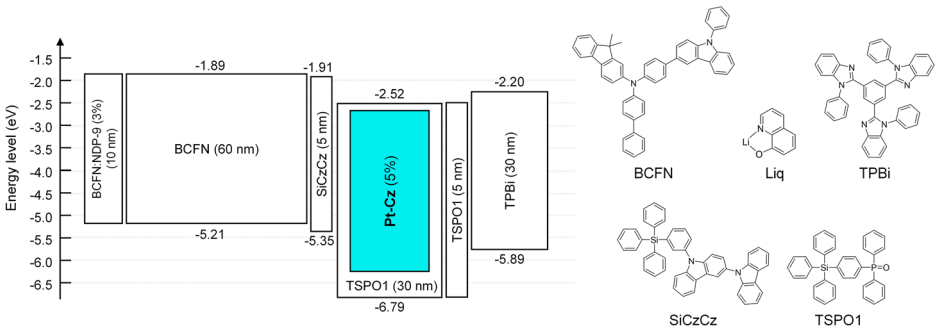

Fig. 9 | OLED device architecture and energy levels. Schematic representation of the OLED device showing energy alignment, materials used, and their corresponding chemical structures.

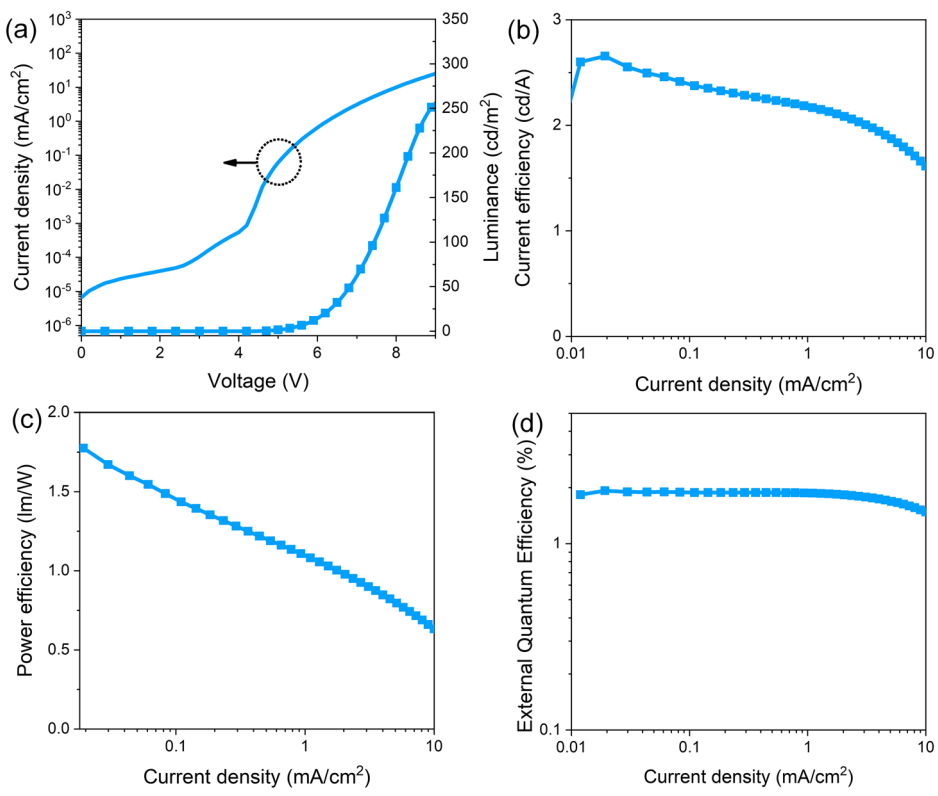

Fig. 10 | Performance characteristics of the Pt-Cz-based OLED device (5 wt% doping). a Current density–voltage–luminance (*J*–*V*–*L*) curves, (**b**) current efficiency (CE) versus current density, (**c**) power efficiency (PE) versus current density, and (**d**) external quantum efficiency (EQE) versus current density profiles.

green electroluminescence (EL) with structured emission peaks in the 460–490 nm range. No emission from the host material or other layers was observed, indicating that all the excitons were confined within the emitting layers. The sky blue OLED doped with 5% Pt-Cz achieved a maximum external quantum efficiency (EQE) of 1.92%, PE of 1.78 lm W^{-1}, and CE of 2.66 cd A^{-1}. The 5%-doped device exhibited structured emission features with emission maxima (λ_{max}) at 410 (sh), 460, and 480 nm, resembling the phosphorescence emission of the Cz unit at 77 K (Fig. 11), which indicated

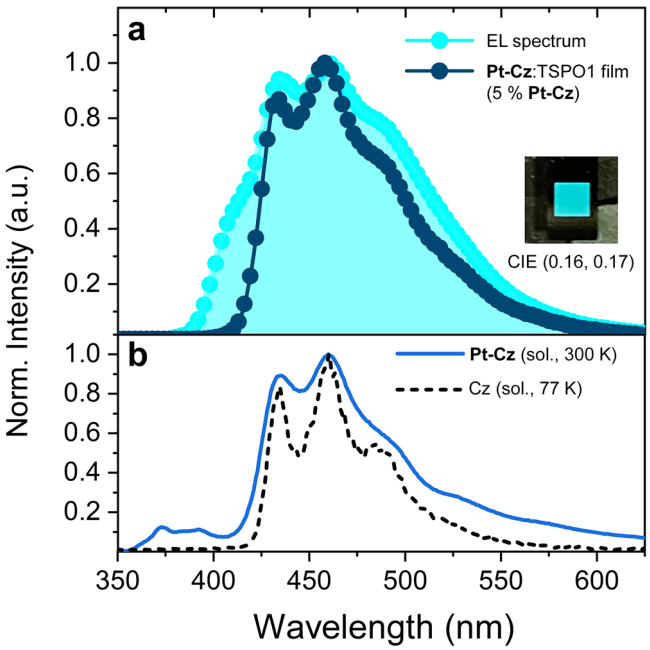

Fig. 11 | Electroluminescence and photoluminescence spectra of Pt-Cz-based device. a Electroluminescence spectrum of Pt-Cz-doped OLED device (sky blue line) and PL spectrum of Pt-Cz:TSPO1 film (5% Pt-Cz) (navy line). **b** Emission spectra of Pt-Cz and the organic Cz fragment measured in dichloromethane at 300 K (blue solid line) and 2-MeTHF at 77 K (black dotted line). Inset: Photograph of the operational OLED emitting sky-blue light.

that triplet emission of tethered Cz (via TTET) was realized in the fabricated OLED device. The 15%-doped device exhibited a significantly broader EL spectrum compared to those of the 5% and 10%-doped devices, centered at 490 nm, and relatively higher EQE, PE, and CE values of 4.4%, 7.5 lm W^{-1}, and 10.5 cd A^{-1}, respectively (Supplementary Figs. 18–19 and Table 8). Overall, as the doping concentration of Pt-Cz in the emitting layer increased, the device efficiency improved; however, the EL spectra shifted toward longer wavelengths with increasing doping concentrations. This behavior is attributed to changes in the electronic structure caused by enhanced intermolecular interactions between Pt-Cz compounds at high doping concentrations (see Supplementary Figs. 19b)[42].

Conclusions

In this study, a peripheral organic group was incorporated into a phenylimidazole (PI)-based Pt(II) complex (Pt^{II}(PI)(acac)) by introducing carbazole (Cz) or naphthalene (Np) substituents at the phenyl ring of the primary PI ligand for the development of persistent organic phosphorescent emitter. The Cz- and Np-tethered complexes Pt-Cz and Pt-Np exhibited exothermic intramolecular triplet-triplet energy transfer (TTET) from the higher ^{3}MLCT state of the Pt core to the lower triplet state (^{3}[LC]*) of the tethered organic Cz or Np moieties, as verified by steady-state photophysical and ultrafast photodynamic studies. Interestingly, the Pt-Cz and Pt-Np showed respectively blue and green phosphorescence of organic periphery groups via TTET process at room-temperature, achieving a reasonable solid-state phosphorescence quantum yield of up to 30%. In the OLED devices fabricated using the developed complexes, the Pt-Cz-doped multilayer system (5% doping) displayed a sky-blue electroluminescent spectrum with CIE coordinates (0.16, 0.17), resembling the structured organic phosphorescence of the Cz unit, thereby confirming that the device emits light from the triplet states of the organic group via TTET. The device achieved an external quantum efficiency (EQE) of 1.92%, a current efficiency of 2.66 cd/A, and a power efficiency of 1.78 lm/W. The developed strategy offers an effective platform for achieving organic phosphorescence emission in OLED applications.

Methods

General

All synthetic procedures were performed under a dry N_2 atmosphere. All solvents used were distilled over sodium benzophenone under N_2 prior to use. The glassware, syringes, magnetic stirrer bars, and needles were dried in a convection oven for at least 8 h. Reactions were monitored using thin-layer chromatography (TLC; Merck Co.) and the products were visualized under UV light (254 or 365 nm). Column chromatography was performed using silica gel 60 G (particle size (5 − 40) μm; Merck Co.). The synthesized compounds were characterized using ^{1}H NMR and Electrospray Ionization mass spectrometry (ESI-MS). ^{1}H NMR spectra were measured on JEOL spectrometer at 400 MHz (JNM-ECZ400S). ESI-MS analysis was performed by the linear ion trap of an LTQ XL ETD mass spectrometer (Thermo FisherScientific, LCQ Fleet Hyperbolic Ion Trap MS/MSn Spectrometer). Absorption and emission spectra at room temperature (RT) were recorded using a UV–Vis spectrophotometer (Agilent, Cary-5000) and fluorimeter (SHIMADZU, RF-6000), respectively. The synthetic routes for the ligand and Pt(II) complexes are provided in Supplementary Scheme 1.

Synthesis

Pt-Cz: $CzPI^+$ (0.7 g, 1.7 mmol) and silver oxide (Ag_2O, 0.2 g, 0.9 mmol) were dissolved in 1,4-dioxane (15 mL) and stirred for 16 h at room temperature. The mixture was then filtered using methanol (MeOH, 30 mL) followed by solvent removal under reduced pressure. The Ag-substituted compound (0.5 g, 0.6 mmol) and dichloro(1,5-cyclooctadiene)platinum(II) (Pt(COD)Cl_2, 0.5 g, 1.2 mmol) were dissolved in 2-ethoxyethanol (15 mL). The mixture was refluxed for 16 h at 130 °C. After cooling and solvent evaporation, the platinized solid residue (Pt(CzPI)Cl_2) was used for the subsequent reaction without further purification. Next, Pt(CzPI)Cl_2 (0.5 g, 0.9 mmol) was dissolved in dimethylformamide (DMF, 45 mL) and subjected to 15 min of N_2 bubbling. Potassium-*tert*-butoxide (*t*-BuOK, 0.4 g, 3.4 mmol) and 2,4-pentanedione (acetylacetone, 0.3 mL, 3.4 mmol) were then added, and the mixture was stirred for 16 h at room temperature, followed by refluxed at 100 °C for 6 h. After the reaction was completed, the residue was filtered with dichloromethane (DCM, 50 mL) and purified by column chromatography using dichloromethane (DCM) and *n*-hexane (Hx). The desired product (Pt-Cz) was obtained from recrystallization using DCM and Hx and dried to afford the product as a beige powder. Yield: 0.15 g (29%).

^{1}H NMR (DMSO-d_6, 400 MHz, δ): 8.25 (d, J = 7.8 Hz, 2H), 8.06 (d, J = 2.1 Hz, 1H), 7.64 (d, J = 2.1 Hz, 1H), 7.57 (d, J = 8.2 Hz, 1H), 7.46 (t, J = 7.6 Hz, 3H), 7.36 (d, J = 8.2 Hz, 2H), 7.29 (t, J = 7.3 Hz, 2H), 7.23 (d, J = 8.0 Hz, 1H), 5.56 (s, 1H), 4.05 (s, 3H), 1.96 (s, 3H), 1.80 (s, 3H) (Supplementary Fig. 1).

^{13}C NMR (Dichloromethane-d_2, 400 MHz, δ): 28.1, 35.4, 102.4, 110.7, 111.4, 115.1, 119.9, 120.6, 121.9, 122.8, 123.5, 126.3, 130.6, 133.4, 142.0, 147.2, 166.9, 185.7. (Supplementary Fig. 2).

ESI-MS (m/z): calcd for $C_{27}H_{23}N_3O_2Pt$: 616.1438, found [M + Na^+] : 638.1705 (Supplementary Fig. 3).

Pt-Np: Pt-Np was synthesized following the same procedure as described above for Pt-Cz, except $NpPi^+$ was used instead of $CzPI^+$. Yield: 0.10 g (19%).

^{1}H NMR (DMSO-d_6, 400 MHz, δ): 8.06 (d, J = 8.7 Hz, 1H), 8.03-7.96 (m, 2H), 7.93 (d, J = 1.0 Hz, 1H), 7.70 (d, J = 7.4 Hz, 1H), 7.61 (d, J = 3.9 Hz, 1H), 7.59 (d, J = 3.9 Hz, 1H), 7.49 (d, J = 8.3 Hz, 1H), 6.99 (d, J = 2.3 Hz, 1H), 6.98 (t, J = 7.6 Hz, 1H), 6.88 (d, J = 7.6 Hz, 1H), 5.94 (d, J = 2.3 Hz, 1H), 5.61 (s, 1H), 3.94 (s, 3H), 2.03 (s, 3H), 1.95 (s, 3H) (Supplementary Fig. 4).

^{13}C NMR (Dichloromethane-d_2, 400 MHz, δ): 28.3, 35.3, 102.3, 118.4, 120.3, 123.8, 126.9, 127.2, 128.3, 128.4, 128.7, 131.2, 133.3, 133.9, 137.8, 144.8, 151.2, 185.8. (Supplementary Fig. 5).

ESI-MS (m/z): calcd for $C_{25}H_{22}N_2O_2Pt$: 577.1329, found [M + Na^+] : 599.1312 (Supplementary Fig. 6).

Theoretical calculations

Density functional theory (DFT) calculations were performed using the Gaussian 09 program package. The ground-state geometry was fully

optimized at the DFT level using the B3LYP (UB3LYP for triplet calculations) method (Supplementary Data 1-1,2). The 6-31 G(d,p) and LANL2DZ basis sets were applied for non-metal atoms and Pt, respectively. Isodensity plots (contour = 0.03 a.u.) of the frontier orbitals were visualized using the Chem3D Ultra or GaussView 6 programs. Time-dependent DFT (TD-DFT) calculations were performed to evaluate the vertical transition energies and oscillator strengths of the singlet and triplet transitions.

Device fabrication and measurement

Indium tin oxide (ITO) was coated onto a glass substrate, and the substrate was cleaned for 15 min each using ultrasonication in acetone, distilled water, and isopropyl alcohol. The cleaned ITO-coated substrate was dried in an oven at 120 °C for 12 h. After that, the dried substrate was treated to O_2 plasma for 2 min under the conditions of 2×10^{-2} Torr and 125 W. The deposition was carried out by thermal evaporation method under high vacuum conditions ($> \sim 10^{-7}$ Torr). The thickness of the deposition was measured by using a quartz crystal monitor, and the deposition rate was controlled to achieve a total of 1 Å/s. The encapsulation process was performed using a glass cap and UV epoxy resin under the conditions of a nitrogen-filled glovebox ($H_2O < 0.1$ ppm, $O_2 < 0.1$ ppm). A getter was attached under the glass cap to absorb any residual moisture or oxygen within the device. The current density (J)–voltage (V) characteristics was measured by injecting current using a source meter (model 2400, Keithley) and the optoelectronic properties including EQE, current efficiency, power efficiency, color coordinates, and electroluminescence (EL) spectra were measured using a chroma meter (CS-2000). The photoluminescence (PL) measurements were conducted using spectrofluorometer (model FS5, Edinburgh Instruments). PL spectra were collected by applying a pulse of 280 nm wavelength through a xenon lamp at room temperature. The 30 nm of solid films (TSPO1 and Pt-Cz or Pt-Np) were deposited on quartz substrates for the PL measurements in the film state.

Data availability

Crystallographic data were deposited with the Cambridge Crystallographic Data Centre as supplementary publications (CCDC-2380466 (Pt-Cz) and CCDC-2381488 (Pt-Np)). Additional crystallographic data are provided in Supplementary Table 1. These data can be obtained free of charge via www.ccdc.cam.ac.uk/data_request/cif, or by e-mailing data_request@ccdc.cam.ac.uk, or by contacting The Cambridge Crystallographic Data Centre, 12 Union Road, Cambridge CB2 1EZ, U.K.; fax: +44 1223 336033. All other relevant data generated and analyzed during this study, which include experimental, spectroscopic, crystallographic and computational data, are included in this article and the Supplementary Data file. X-ray crystal structure cif files for Pt-Cz (Supplementary Data 6) and Pt-Np (Supplementary Data 7) are attached.

Received: 12 October 2024; Accepted: 22 April 2025;
Published online: 09 May 2025

References

1. Tang, C. W. & VanSlyke, S. A. Organic electroluminescent diodes. *Appl. Phys. Lett.* **51**, 913–915 (1987).
2. Baldo, M. A. et al. Highly efficient phosphorescent emission from organic electroluminescent devices. *Nature* **395**, 151–154 (1998).
3. D. J. Gaspar & E. Polikarpov. OLED fundamentals. In *Materials, Devices, and Processing of Organic Light-Emitting Diodes* (eds. Gaspar, D. J., Polikarpov, E.) 494 (CRC Press, Boca Raton, 2015).
4. Yersin, H. *Highly Efficient OLEDs With Phosphorescent Materials* (Wiley-VCH: Weinheim, 2008).
5. Stephen R. F "Breaking the lifetime barrier for deep blue phosphorescent OLEDs". In *Proc. SPIE 13122, Organic and Hybrid Light Emitting Materials and Devices XXVIII,* 1312202 (IEEE, 2024).
6. Longhi, E. & Cola, L. D. Iridium(III) complexes for OLED application. In *Iridium(Iii) In Optoelectronic And Photonics Applications*. (ed. Colman, E. Z.) (John Wiley & Sons, Ltd: 2017).
7. Chi, Y. & Chou, P.-T. Transition-metal phosphors with cyclometalating ligands: fundamentals and applications. *Chem. Soc. Rev.* **39**, 638–655 (2010).
8. Xiao, L. et al. Recent progresses on materials for electrophosphorescent organic light-emitting devices. *Adv. Mater.* **23**, 926–952 (2011).
9. Fu, H., Cheng, Y.-M., Chou, P.-T. & Chi, Y. Feeling blue? blue phosphors for OLEDs. *Mater. Today* **14**, 472–479 (2011).
10. Zhang, Y., Lee, J. & Forrest, S. R. Tenfold increase in the lifetime of blue phosphorescent organic light-emitting diodes. *Nat. Commun* **5**, 5008–5014 (2014).
11. Lee, J. et al. Hot excited state management for long-lived blue phosphorescent organic light-emitting diodes. *Nat. Commun.* **8**, 15566 (2017).
12. Kim, S. et al. Degradation of bluephosphorescent organic light-emitting devices involves excitoninduced generation of polaron pair within emitting layers. *Nat. Commun.* **9**, 1211 (2018).
13. Uoyama, H., Goushi, K., Shizu, K., Nomura, H. & Adachi, C. Highly efficient organic light-emitting diodes from delayed fluorescence. *Nature* **492**, 234–238 (2012).
14. Zhang, Q. et al. Efficient blue organic light-emitting diodes employing thermally activated delayed fluorescence. *Nat. Photon* **8**, 326–332 (2014).
15. Tang, X. et al. Highly efficient luminescence from space-confined charge-transfer emitters. *Nat. Mater.* **19**, 1332–1338 (2020).
16. Goushi, K., Yoshida, K., Sato, K. & Adachi, C. Organic light-emitting diodes employing efficient reverse intersystem crossing for triplet-to-singlet state conversion. *Nat. Photon.* **6**, 253–258 (2012).
17. Hu, Y. X. et al. Efficient selenium-integrated TADF OLEDs with reduced roll-off. *Nat. Photonics* **16**, 803–810 (2022).
18. Liu, Y., Li, C., Ren, Z., Yan, S. & Bryce, M. R. All-organic thermally activated delayed fluorescence materials for organic light-emitting diodes. *Nat. Rev. Mater.* **3**, 18020 (2018).
19. Li, T.-Y., Zheng, S.-J., Djurovich, P. I. & Thompson, M. E. Two-coordinate thermally activated delayed fluorescence coinage metal complexes: molecular design, photophysical characters, and device application. *Chem. Rev.* **124**, 4332–4392 (2024).
20. Mongin, C., Moroz, P., Zamkov, M. & Castellano, F. N. Thermally activated delayed photoluminescence from pyrenyl-functionalized CdSe quantum dots. *Nat. Chem.* **10**, 225–230 (2018).
21. Tanner, P. A., Zhou, L., Duan, C. & Wong, K.-L. Misconceptions in electronic energy transfer: bridging the gap between chemistry and physics. *Chem. Soc. Rev.* **47**, 5234–5265 (2018).
22. Hirata, S., Totani, K., Yamashita, T., Adachi, C. & Vacha, M. Large reverse saturable absorption under weak continuous incoherent light. *Nat. Mater.* **13**, 938–946 (2014).
23. Breen, D. E. & Keller, R. A. Intramolecular energy transfer between triplet states of weakly interacting chromophores. I. Compounds in which the chromophores are separated by a series of methylene groups. *J. Am. Chem. Soc.* **90**, 1935–1940 (1968).
24. Polosan, S., Ciobotaru, I. C. & Tsuboi, T. Absorption, phosphorescence and raman spectra of $IrQ(ppy)_2$ organometallic compound. *Mater. Chem. Phys.* **162**, 822–830 (2015).
25. Kumar, S., Hisamatsu, Y., Tamaki, Y., Ishitani, O. & Aoki, S. Design and synthesis of heteroleptic cyclometalated iridium(III) complexes containing quinoline-type ligands that exhibit dual phosphorescence. *Inorg. Chem.* **55**, 3829–3843 (2016).
26. López-López, J. C., Bautista, D. & González-Herrero, P. Stereoselective formation of facial tris-cyclometalated Pt^{IV} complexes: dual phosphorescence from heteroleptic derivatives. *Chem. Eur. J.* **26**, 11307–11315 (2020).
27. You, Y. et al. Phosphorescent sensor for robust quantification of copper(II) ion. *J. Am. Chem. Soc.* **133**, 11488–11491 (2011).
28. Wei, Y. et al. Efficient triplet−triplet annihilation upconversion in solution and hydrogel enabled by an S-T absorption Os(II) complex

dyad with an elongated triplet lifetime. *Inorg. Chem.* **60**, 19001–19008 (2021).
29. Hamze, R. et al. Eliminating nonradiative decay in Cu(I) emitters: >99% quantum efficiency and microsecond lifetime. *Science* **363**, 601–606 (2019).
30. Bilen, C. S., Harrison, N. & Morantz, D. J. Unusual room temperature afterglow in some crystalline organic compounds. *Nature* **271**, 235 (1978).
31. Mu, Y. et al. Mechano-induced persistent room-temperature phosphorescence from purely organic molecules. *Chem. Sci.* **9**, 3782–3787 (2018).
32. Paul, L., Chakrabarti, S. & Ruud, K. Origin of dual-peak phosphorescence and ultralong lifetime of 4,6-diethoxy-2-carbazolyl-1,3,5-triazine. *J. Phys. Chem. Lett.* **8**, 1253–1258 (2017).
33. Zhao, W. et al. Boosting the efficiency of organic persistent room-temperature phosphorescence by intramolecular triplet-triplet energy transfer. *Nat. Commun.* **10**, 1595 (2019).
34. Molecular packing: another key point for the performance of organic and polymeric optoelectronic materials. *Acc. Chem. Res*. **53**, 962–973 (2020).
35. Zhao, W. et al. Highly sensitive switching of solid-state luminescence by controlling intersystem crossing. *Nat. Commun.* **9**, 3044 (2018).
36. He, Z. et al. White light emission from a single organic molecule with dual phosphorescence at room temperature. *Nat. Commun.* **8**, 416 (2017).
37. Yuan, W. Z. et al. Crystallization-induced phosphorescence of pure organic luminogens at room temperature. *J. Phys. Chem. C* **114**, 6090 (2010).
38. Unger, Y. et al. Green–blue emitters: NHC-based cyclometalated [Pt(C^C*)(acac)] complexes. *Angew. Chem. Int. Ed.* **49**, 10214–10216 (2010).
39. Turro, N. J., Ramamurthy, V. & Scaiano, J. C. *Modern Molecular Photochemistry Of Organic Molecules*, Vol 1084 (University Science Books, 2010).
40. Chon, B. et al. Investigation of interface characteristics and physisorption mechanism in quantum dots/TiO_2 composite for efficient and sustainable photoinduced interfacial electron transfer. *ACS Appl. Mater. Interfaces* **16**, 9414–9427 (2024).
41. Lee, J. et al. Deep blue phosphorescent organic light-emitting diodes with very high brightness and efficiency. *Nat. Mater.* **15**, 92–98 (2016).
42. Guijie, L. et al. Tetradentate platinum(II) complexes for highly efficient phosphorescent emitters and sky blue OLEDs. *Chem. Mater.* **32**, 537–548 (2020).

Acknowledgements

We thank the Cooperative Center of Hongik University for the NMR measurements and Dr. So-Yoen Kim for help with the synthesis of CzPI and CzNp. This work was supported by the National Research Foundation of Korea (NRF) funded by the Ministry of Education (NRF-2019R1F1A1061497), the Ministry of Trade, Industry, and Energy (MOTIE) of the Republic of Korea (RS-2024-00418716), and the Korean Government (MSIT) (RS-2025-00562897).

Author contributions

S. W. Jeong: Materials synthesis and characterization, formal analysis, investigation, data curation, writing–review and editing, visualization. H. J. Lee: Photodynamic analysis, investigation, writing–review and editing, visualization. B. J. Park: OLED device fabrication, investigation, writing–review and editing, visualization. M.-J. Bong: X-ray analysis, investigation, writing–review and editing, visualization. D. Lee: DFT calculation, investigation, writing–review and editing, visualization. T. Kim: Experiment design, investigation, data curation, writing–review and editing, supervision. C. H. Kim: Photodynamic analysis, investigation, data curation, writing–review and editing, supervision. H.-J. Son: Resources, writing–review and editing, supervision, project administration, funding acquisition. All authors have read and agreed to the published version of the manuscript.

Competing interests

The authors declare no competing interests.

Additional information

Supplementary information The online version contains supplementary material available at https://doi.org/10.1038/s42004-025-01533-y.

Correspondence and requests for materials should be addressed to Taekyung Kim, Chul Hoon Kim or Ho-Jin Son.

Peer review information *Communications Chemistry* thanks Kang Mun Lee and the other, anonymous, review for their contribution to the peer review of this work. Peer review reports are available.